Distributed Temperature Sensing for Oceanographic Applications

Article · October 2020 DOI: 10.1175/JTECH-D-20-0066.1			
DOI: 10.117	/31EUH-1/-20-0006.1		
CITATIONS 0	<u> </u>	READS 12	
7 authors, including:			
6	Gregory Sinnett University of California, Irvine 7 PUBLICATIONS 51 CITATIONS SEE PROFILE		
Some of the authors of this publication are also working on these related projects:			
Drainet	The Nearshore Heat Budget View project		

⁶Distributed Temperature Sensing for Oceanographic Applications

Gregory Sinnett, ^a Kristen A. Davis, ^a Andrew J. Lucas, ^b Sarah N. Giddings, ^b Emma Reid, ^a Madeleine E. Harvey, ^b and Ian Stokes

^a University of California, Irvine, Irvine, California; ^b University of California, San Diego, La Jolla, California

(Manuscript received 4 May 2020, in final form 27 August 2020)

ABSTRACT: Distributed temperature sensing (DTS) uses Raman scatter from laser light pulsed through an optical fiber to observe temperature along a cable. Temperature resolution across broad scales (seconds to many months, and centimeters to kilometers) make DTS an attractive oceanographic tool. Although DTS is an established technology, oceanographic DTS observations are rare since significant deployment, calibration, and operational challenges exist in dynamic oceanographic environments. Here, results from an experiment designed to address likely oceanographic DTS configuration, calibration, and data processing challenges provide guidance for oceanographic DTS applications. Temperature error due to suboptimal calibration under difficult deployment conditions is quantified for several common scenarios. Alternative calibration, analysis, and deployment techniques that help mitigate this error and facilitate successful DTS application in dynamic ocean conditions are discussed.

KEYWORDS: In situ oceanic observations; Instrumentation/sensors

1. Introduction

Dynamic oceanographic processes act over a wide temporal and spatial range, from turbulence (small and fast) to climate (large and slow). Observing across these broad scales helps account for the full dynamics of a complex ocean. However, instrument limitations (battery, memory, response time, etc.) often limit possible temporal scales, and many cosampling instruments or advanced equipment (such as gliders, drifters, or profilers) are often required to broaden spatial resolution. Distributed temperature sensing (DTS) systems are attractive due to their ability to continuously sample at relatively high temporal and spatial resolution for significant duration over broad spatial scales. Although DTS use in environmental applications has increased since 2006, application to oceanography is complex and still relatively rare (Shanafield et al. 2018).

DTS systems observe the Raman scatter from laser light pulsed through an optical fiber to observe its temperature. Sensitive electronics and laser equipment require protection from the elements and continuous power to operate, and delicate fibers connected to the device should not be bent or crimped. Further, DTS calibration requires independent temperature observations along parts of the cable (e.g., Hausner et al. 2011). Despite these challenges, temperature observation with DTS has been successfully accomplished in several environmental settings, including lakes (e.g., Selker et al. 2006b), rivers (e.g., Selker et al. 2006a), groundwater (Read et al. 2013), estuaries (e.g., Henderson et al. 2009; Harvey 2019), canals (e.g., Neilson et al. 2010), snowpack (e.g., Tyler et al. 2008), under glacial ice shelves (e.g., Tyler et al. 2013; Kobs et al. 2014), volcanoes (e.g., Curtis and Kyle 2011), and the

Oenotes content that is immediately available upon publication as open access.

Corresponding author: Gregory Sinnett, gsinnett@uci.edu

atmosphere (e.g., Zeeman et al. 2015). Although improvements to DTS ruggedization and power requirements have aided field deployments, significant challenges still exist in dynamic oceanographic settings. Recently, DTS has been used to supplement oceanographic studies, though remote and difficult environmental conditions often complicate the deployment and analysis (Connolly and Kirincich 2019; Reid et al. 2019; Davis et al. 2020).

This experiment was designed to address common challenges inherent in oceanographic DTS deployments. Two different DTS systems, three different cables and 24 thermistors were used to test aspects of the DTS systems and cables, as well as various calibration configurations. Results are intended to aid future oceanographic DTS deployments and provide guidance for obtaining the best possible temperature signal in challenging deployment and operational conditions. The experiment location and deployment are described in section 2, and DTS theory and typical methods are described in section 3. Example cable selection options and their temperature response time are provided in section 4. Section 5 contains results related to various practical calibration challenges, including calibrating with single points (rather than sections), calibrating with small temperature differences, and calibrating when a section of the cable is lost or damaged. Section 6 addresses data processing techniques including noise reduction, locating boundaries (between air and water for example), and cable burial using DTS temperature data. Section 7 summarizes the key findings.

2. Experiment description

a. Site

DTS temperature observations were made adjacent to the Scripps Institution of Oceanography (SIO) pier in La Jolla, California, from 26 October to 5 November 2018. The SIO pier terminates in water depth $h \approx 8 \text{ m}$ (Fig. 1). Sandy bathymetry

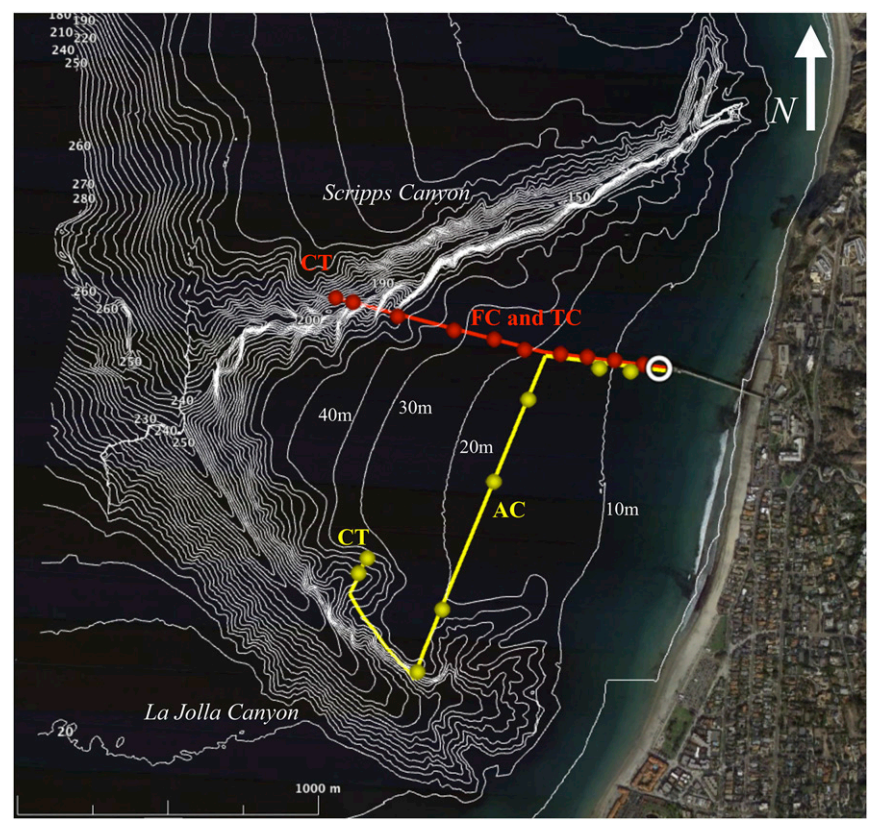


FIG. 1. Google Earth image of Scripps Beach and the La Jolla canyon system (32.867°N, -117.257°E) with 10 m contours. Scripps Canyon extends northeastward and La Jolla Canyon extends southeastward. FC and TC cables were deployed along the red track, and the AC cable was deployed along the yellow track. Validation point and terminus coil CT locations (dots), and locations of additional reference sections C1 and C2 (white circle) are approximate.

continues offshore with slope $s \approx 0.033$ to $h \approx 30 \,\mathrm{m}$, where depths then increase rapidly into Scripps Canyon ($h \approx 200 \,\mathrm{m}$). The shallow region south of the SIO pier is roughly alongshore uniform for $\approx 1 \,\mathrm{km}$.

b. Experiment design

A temperature controlled shed at the end of the SIO pier housed and provided power for two different DTS instruments used in this experiment. A Silixa XT-DTS and a Silixa ULTIMA DTS sampled three different cables (selected for their various physical properties) all originating from the pier end. They included 1) a 2 km long, 6 mm outside diameter Kaiphone armored cable (denoted here as "AC") containing two multimode fibers set inside a stainless steel flexible tube, aramid yarn, stainless steel braiding and an outer jacket; 2) a 2 km Optical Fiber Solutions mini LT Flat Drop cable (denoted here as "FC") containing two multimode fibers encased between two fiberglass strength members and polyethylene jacket; and 3) a very light and flexible 2.2 mm outside diameter "tactical" cable (denoted here as "TC") containing a single multimode fiber encased in Kevlar and waterproof coating.

These cables were selected for their relatively light construction and ability to be deployed from small nearshore

watercraft. Heavier cables containing steel tube construction provide enhanced protection from tensile stresses and may be more suitable for deep sea application. Cable construction affects both the temperature response time (see section 4) and cable behavior in the water, and should be carefully considered before oceanographic DTS deployments. The AC cable was the densest, occasionally burying several centimeters in the sand, especially where surface waves were strong enough to suspend sediment. The FC was less dense, sinking to the bottom but rarely becoming buried, while the flexible tactical cable was nearly neutrally buoyant and joined with tape to the FC cable every 30.5 m to provide rigidity.

All three cables were deployed from a small vessel using a spool secured to the aft deck. With the vessel making headway speed and continually recording a GPS track, a crew of at least four allowed the cable to unspool while recording cable meter marks (previously printed on the cable), depths and GPS coordinates. To record accurate temperature at specific points along the cable, seven RBR SoloT or SeaBird SBE56 temperature sensors (both 0.002°C accuracy) were attached to the AC cable (yellow track, Fig. 1) during deployment using zip ties and electrical tape at premarked validation locations V1–V7 (Fig. 2a, and yellow dots, Fig. 1). Nine RBR SoloT or SeaBird SBE56

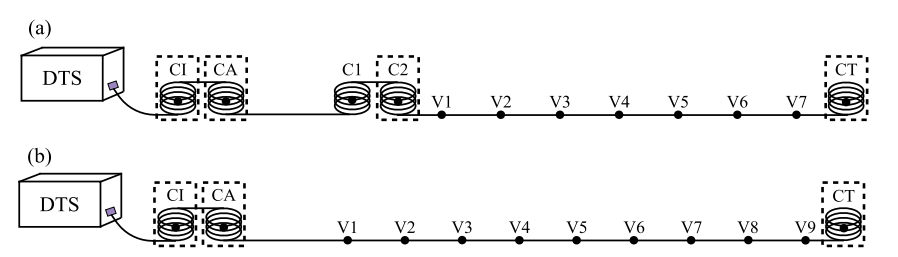


FIG. 2. Schematic cable layout for (a) the AC cable and (b) the FC and TC cables. Relative locations of the 10 m coiled calibration sections (coils), validation points (dots), and cooler locations (boxed dots) are not to scale.

temperature sensors were also attached to the FC and TC cables (red track, Fig. 1) at validation locations V1–V9 (Fig. 2b, and red dots, Fig. 1). Each high-accuracy RBR SoloT or SeaBird SBE56 temperature sensor sampled at 1 Hz. Equipment was recovered by navigating over the recorded ship track and respooling the cable. Actual cable location is difficult to pinpoint and depends on many factors such as ocean current during deployment, bathymetric irregularities, and any cable movement after deployment. Recording both the deployment and recovery ship track, and diving to inspect the cable (where possible) reduced uncertainty in the cable's location.

Coiled 10 m sections of cable and multiple colocated thermistors were included to calibrate and validate the DTS temperature signal (Fig. 2). After exiting the pier-end shed, all three cables were coiled in an ice bath cooler (section CI, Fig. 2) then in a cooler containing ambient water (section CA, Fig. 2) on the pier deck. During the experiment, ice was continually supplied to the cooler containing CI for all three cables. Cables then passed through strain relief and down a piermounted conduit into the water where they were secured to a pier piling, then a sand anchor near the base of the pier, before extending westward along the bottom. Within 20 m of the pierend sand anchor, two additional experimental calibration coils were included on the AC cable. Section C1 was coiled directly on the sandy bottom, and section C2 was coiled inside a soft cooler bag (Fig. 2a); both were secured in place with sand anchors.

Dives on 26 October, 29 October, and 4 November were made along the cable section from the pier end to $h \approx 20\,\mathrm{m}$ (square, Fig. 1) to inspect the cables, noting any burial, crimping or cable strain points and general cable location. Except where noted, results focus on a 3-day time period between 27 and 30 October when the Silixa XT-DTS was sampling all fibers with 10 s and 0.25 m resolution.

3. DTS theory and application

a. Theory

DTS systems pulse laser light through a fiber optic cable to observe the returned Raman scattered light. Raman scattering takes place when an incident photon with angular frequency ω_0 either excites a particle in the ground state which emits a photon while returning to a vibrational state (Stokes scattering), or excites a particle in a vibrational state which emits a photon while returning to the ground state (anti-Stokes scattering).

For a vibrational state at an elevated energy ΔE , the scattered photons have angular frequency $\omega = \omega_0 \pm \Delta E/\hbar$ where \hbar is Planck's constant. Stokes scattered photons have lost energy, and anti-Stokes scattered photons have gained energy relative to the incident photon. The probability of a particle existing in a given energy state is given by the Boltzmann distribution

$$P_i \propto e^{-E_i/(k_b T)},\tag{1}$$

where E_i is the energy of that state, k_b is the Boltzmann constant, and T is the temperature. Thus, the ratio of Stokes to anti-Stokes backscatter intensities is

$$\frac{P_s}{P_{-s}} = e^{\Delta E/(k_b T)},\tag{2}$$

where P_S and P_{aS} are the observed Stokes and anti-Stokes backscatter intensities, respectively. Readers are referred to Farahani and Gogolla (1999), Selker et al. (2006b), and Tyler et al. (2009) for further examples of DTS optical theory.

From Eq. (2), temperature (unit: K) along the cable at distance d is often expressed (e.g., van de Giesen et al. 2012) as

$$T(d,t) = \frac{\gamma}{\ln \frac{P_S(d,t)}{P_S(d,t)} + C(t) - \int_0^d \Delta \alpha(d',t) \, dd'}.$$
 (3)

Here, the difference in energy states are related by

$$\gamma = \Delta E/k_b, \tag{4}$$

where γ has units of K, C is a calibration parameter related to properties of the laser light and the DTS instrument, and $\Delta\alpha$ (m⁻¹) is the differential attenuation between the anti-Stokes and Stokes signal (Hausner et al. 2011; Connolly and Kirincich 2019). The Stokes and anti-Stokes backscatter intensities (P_S and P_{aS} , respectively) are found along the cable distance d from time-of-flight observation. The free parameters in Eq. (3) [γ , C(t) and $\Delta\alpha(d',t)$], are optimally determined for double-ended cable deployments (where the DTS samples a looped fiber from both directions) by calibration routine (e.g., van de Giesen et al. 2012).

A wide range of deployment considerations exist (Tyler et al. 2009) and enabling a double-ended cable deployment by splicing a duplex cable (containing two fibers) is not always possible or advantageous. Dynamic ocean conditions may damage a splice or a section of cable, and many ocean applications

benefit from measuring the entire length of a single-ended deployment (where the DTS samples a single fiber in one direction) using the highest DTS power and cable length possible. For these single-ended deployments, $\Delta \alpha$ is commonly assumed constant along the cable. Equation (3) becomes

$$T(d,t) = \frac{\gamma}{\ln \frac{P_{S}(d,t)}{P_{\alpha S}(d,t)} + C(t) - \Delta \alpha(t)d}.$$
 (5)

The same three free parameters in Eq. (5) [γ , C(t), and $\Delta\alpha(t)$] are again found by calibration routine (e.g., Hausner et al. 2011). Here, we optimize this single-ended deployment configuration for ocean applications.

b. Standard calibration procedure

Three known temperatures at known distances along the cable are required to solve for the three free parameters in Eq. (5). To fully constrain the free parameters, temperatures used to calibrate the DTS signal should span the entire observed temperature range along the cable length and include observations near the start and end of the cable. Calibration between sections at the start and end of the cable constrains $\Delta \alpha$, and an additional calibration section at a different temperature provides the third constraint required to solve Eq. (5). Minimizing the distance between the calibration sections held at different temperatures (thus reducing the effect of attenuation $\Delta \alpha$) minimizes error propagation from $\Delta \alpha$ estimates. Calibration is typically achieved by passing a coiled section of cable through both an ice bath and a warm bath of known temperature near the DTS instrument, while also independently measuring temperature at the terminal end. Following Hausner et al. (e.g., 2011), all three cable calibration sections and associated loggers are used to solve the system of equations required to estimate T(d, t) for single-ended cables.

The standard calibration routine described above assumes that differential attenuation $\Delta\alpha$ is constant along the entire cable length. This assumption is not necessarily true, as cable imperfections, sharp bends and strain can cause variation in optical properties (Tyler et al. 2009; Hausner and Kobs 2016) and gradual losses can occur when the cable is bent or curved (Arnon et al. 2014). For example, the differential attenuation near the start of the cable in this deployment is likely different from the rest of the cable due to the multiple coiled calibration sections, sand anchors and bends required to secure and guide the cable from the pier station to the ocean floor.

Empirical corrections for variable differential attenuation in a helically wound cable have reduced temperature error by ≈ 0.5 °C (Arnon et al. 2014). Here, we take a similar empirical approach to estimate $\Delta\alpha(d')$ and use the full Eq. (3) rather than Eq. (5). The variable $\Delta\alpha(d')$ is estimated along the single-ended cable by assuming temperature, γ , and C remain constant at adjacent locations (small Δd). Following Hausner et al. (2011), and with these assumptions, rearranging Eq. (3) yields

$$\Delta\alpha(d') = \frac{\ln \frac{P_S(d' + \Delta d)}{P_{aS}(d' + \Delta d)} - \ln \frac{P_S(d')}{P_{aS}(d')}}{\Delta d}.$$
 (6)

As observations of P_S and P_{aS} are inherently noisy, $\Delta \alpha(d')$ is also noisy and affected by variable strain caused by cable bending. However, any systemic $\Delta\alpha(d')$ differences from constant strain at a fixed point (such as a sand anchor or calibration loop) likely persist after the cable is placed. To correct for attenuation differences between the first 85 m (defined d1, containing the majority of the coils and bends) and the remaining 2915 m (defined d2), a long-time-average differential attenuation was found for $\langle \Delta \alpha_{d1} \rangle$, $\langle \Delta \alpha_{d2} \rangle$ and for the entire cable $\langle \Delta \alpha_c \rangle$. The long-time-averaged ratios $\langle \Delta \alpha_{d1} \rangle / \langle \Delta \alpha_c \rangle$ and $\langle \Delta \alpha_{d2} \rangle / \langle \Delta \alpha_c \rangle$ were used to scale $\Delta \alpha_{d1}(t)$ and $\Delta \alpha_{d2}(t)$, respectively. The resulting modified differential attenuation in each section was then combined to form a piecewise linear function of $\Delta\alpha(d',t)$ used in Eq. (3). Adjusting for inconsistent $\Delta \alpha$ along the cable in this way improved the average temperature bias from 0.33° to 0.05°C. Two sections were used in this case to form the piecewise fit; however, using more than two sections may be advantageous if $\Delta \alpha$ is expected to consistently change in three or more sections. Increasing the number of sections will decrease the available $\Delta \alpha$ averaging, however.

c. Optimally calibrated DTS observation and error

When calibrated, DTS is a powerful tool capable of resolving temperature across broad spatial and temporal scales. For example, DTS-observed temperature from the pier end to Scripps Canyon (see red line, Fig. 1) during a 3-day period between 27 and 30 October contains internal tidal oscillations (Fig. 3a) which are typical of the region (Alberty et al. 2017; Sinnett et al. 2018). Coherently propagating temperature features are present and can be observed by DTS at both large and small scales (Fig. 3b). However, DTS error is not constant and is occasionally poorly constrained, motivating a detailed understanding of DTS skill in many different situations.

DTS temperature error at each validation point $T_{\text{err}}^i = T_i - T_{\text{V}i}$ establishes the instrument skill, where T_i is the observed cable temperature at the validation point i and T_{Vi} is the "true" temperature from the high accuracy stand-alone temperature sensors. Validation temperatures T_{Vi} are temporally averaged to match the DTS resolution. As a typical example, averaged temperature at validation point V3 on cable FC ($d = 406 \,\mathrm{m}$) varied between $T_{V3} = 13.95^{\circ}$ and 19.02° C (red, Fig. 3c). When optimally calibrated with CI, CA, and CT, and after making the piecewise linear adjustment to $\Delta \alpha$, the FC cable temperature at validation point 3, T_3 , tracked colocated T_{V3} with 10 s temporal resolution and 0.25 m spatial resolution and root-mean-square error RMSE = 0.07°C (black, Fig. 3c). Such optimal calibration conditions are not always possible in field settings, and reducing noise (at the expense of spatial or temporal resolution) may at times be necessary. The following sections quantify influences to the DTS skill under various calibration and deployment challenges, and provide guidance for minimizing noise, visible as very high-frequency variability (black, Fig. 3c).

4. Cable response time

There are many cable construction options to consider, such as cladding, fiber protection, strength members, additional armoring, coatings, and markings. Sensing environmental

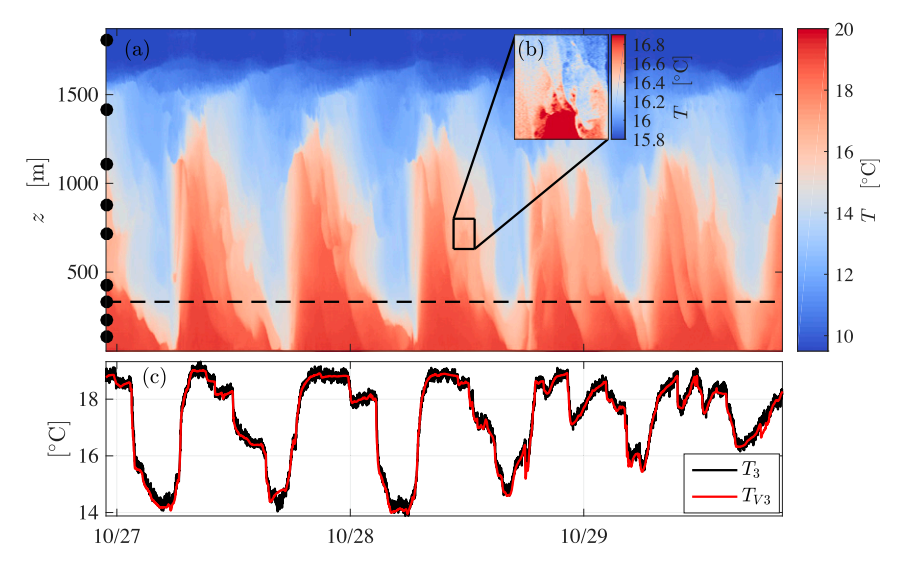


FIG. 3. (a) Temperature (color bar) observed by the FC cable along its nearly 2 km length and over the 3-day experimental period. Locations of independent validation thermistors are indicated by black dots, and the location of validation point 3 is dotted. (b) This inset is rescaled showing 170 m over 2 h with a 1°C temperature range to highlight small-scale features observed by the DTS. (c) DTS temperature at validation point 3 T_3 (black) and colocated independently observed validation temperature $T_{\rm V3}$ (red), each averaged to have 10 s resolution.

temperature with a cable depends on the cable's fiber maintaining thermal equilibrium with the environment. Thus, DTS temporal resolution depends on the cable construction, since thermal response time varies for cables containing different materials (Tyler et al. 2009). Here, we use a fast-sampling (1 Hz resolution) Silixa Ultima DTS to test the response time of the FC and TC cables (see section 2b). DTS temperature observations were calibrated following the best-practice method in section 3b.

Cable sections were repeatedly exposed to and allowed to equilibrate in air (\approx 25°C), in an ambient water bath (\approx 17°C), and an ice bath (\approx 0°C) before being removed to the air again to generate steplike temperature changes. Actual air, water and ice bath temperature were observed by thermistors and used to normalize the exponential DTS temperature response ($R^2 > 0.92$ in all cases). Cable response time was derived from the normalized e-folding time of the repeated trials (N > 30). In water, the FC mean and standard deviation response time is 12 ± 3 s, while the thinner TC response time is 6 ± 1 s in water. In air, response times were 12 to 20 times higher (with larger standard deviation) due to the significantly lower thermal conductivity of air.

Cable selection is a primary choice which informs deployment options, data processing and ultimately the data quality. Selecting a cable that satisfies deployment constraints and is optimized for strain and thermal response time considerations often involves some compromise. Section 5 addresses various calibration challenges using the AC cable (Fig. 2a) which contained additional calibration sections designed for this experiment. Section 6 addresses data processing techniques using the FC cable (Fig. 2b) which was conventionally deployed with additional validation measurements.

5. Deployment and calibration

a. Single point calibration

Reducing P_S and P_{aS} noise within a calibration section improves calibration and subsequent temperature accuracy along the cable length. Maintaining a cable section at a known temperature, then averaging the Stokes and anti-Stokes signals in that section is a common noise reduction method and aids calibration accuracy. For example, Hausner et al. (2011) observed $\approx 0.05^{\circ}$ C RMSE improvement when reference sections were long enough to average at least 10 adjacent observations. In the field, lengthy calibration sections may be difficult to create or maintain, and a calibration "point" (or section of significantly shorter length) may be required instead.

Calibrating the AC cable using single points (rather than the calibration sections used in section 3b) caused RMSE to increase at all validation points. However, there was generally larger RMSE increase at points further away from the DTS with lower P_S (Fig. 4). Yet, the overall RMSE increase was relatively small, between 0.02° and 0.05°C and bias was nearly unaffected (not shown), indicating that single point calibrations are possible with only a slight increase in error. This extra error may be minimized if DTS power is increased or analysis is limited to parts of the cable with strong P_S .

b. Calibration with small temperature differences

Equations (3) and (5) are optimally constrained if calibration section temperatures span a wide range and bound temperatures observed along the cable length. To accomplish this, field DTS deployments commonly use an ice bath and a warm

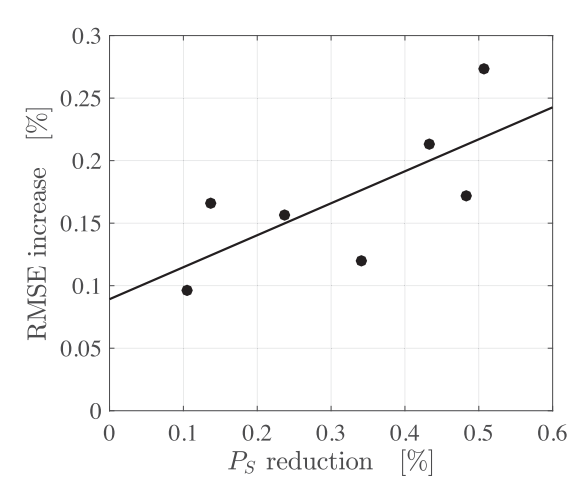


FIG. 4. RMSE increase due to calibration using single points (rather than calibration sections) vs Stokes backscatter intensity relative to the start of the cable. The RMSE is generally higher at reduced P_S (larger d), with best-fit line slope of 0.26, intercept of 0.09, and $R^2 = 0.51$.

(ambient) bath as two of the three calibration sections, though sometimes the ice bath cannot be maintained in the field, or the calibration bath temperature cannot be controlled (e.g., Connolly and Kirincich 2019). Effects on the DTS skill caused by calibrating with a small calibration section temperature difference [causing Eqs. (3) and (5) to be suboptimally constrained] are tested here using the Silixa XT-DTS system sampling the AC cable at 0.25 m intervals with a 10 s acquisition time.

DTS temperature calibration used the standard calibration routine (section 3b) with both large and small calibration section temperature differences over the same time period. The calibration temperature difference is $\Delta T_{\rm cal}$ = $|T_{\text{Cexp}} - T_{\text{CA}}|$ where T_{Cexp} is an "experimental" calibration temperature and T_{CA} is the ambient calibration (see Fig. 2). The standard calibration method (section 3b) uses the ice bath (Cexp = CI). However, an alternative calibration section Cexp = C2 located in situ ($h \approx 10 \,\mathrm{m}$, see Fig. 2a) was contained in a soft cooler simulating a nontemperature-controlled bath as might be the case if the ice bath could not be maintained. When $\Delta T_{\rm cal}$ is small (as was often the case with the alternative calibration setup), DTS temperature calibration is poorly constrained over the observed temperature range. An alternative calibration procedure is developed for these cases.

1) Calibration effects with small $\Delta T_{\rm cal}$

Using the standard calibration setup with a temperature controlled ice bath, $\Delta T_{\rm cal}=17.8^{\circ}\pm1.4^{\circ}{\rm C}$ with $\Delta T_{\rm cal}$ never below 12.7°C over the 3-day observational period. When calibrated with this large $\Delta T_{\rm cal}$, the root-mean-square error and bias at validation points V1 to V7 was small and consistent (black symbols, Fig. 5), with $\overline{\rm RMSE}=0.19^{\circ}\pm0.04^{\circ}{\rm C}$ and bias $\overline{b}=0.02^{\circ}\pm0.07^{\circ}{\rm C}$, respectively. Here statistics are applied to the 3-day time series and the overbar represents an average of the seven validation points.

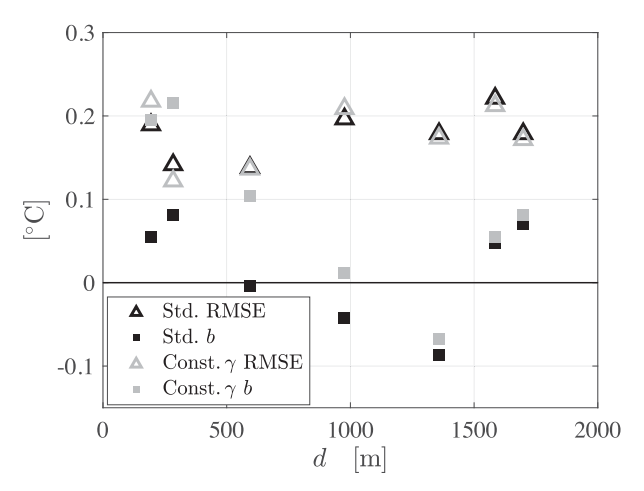


FIG. 5. Root-mean-square error (RMSE, triangles) and bias (b, squares) at validation points along the AC cable distance d comparing calibration with large ΔT_{cal} (dark symbols) to calibration with small ΔT_{cal} and constant γ (light symbols).

The alternative calibration (using C2 instead of the ice bath CI) significantly reduced the calibration temperature difference, with $\Delta T_{\rm cal}$ ranging from 0° to 3.27°C. When calibrated using this small $\Delta T_{\rm cal}$, Eq. (5) is poorly constrained, and $\overline{\rm RMSE}=33.78^{\circ}\pm30.86^{\circ}{\rm C}$ and large $T_{\rm err}=1.22^{\circ}\pm44.23^{\circ}{\rm C}.$ Calibrating with a small $\Delta T_{\rm cal}$ also resulted in unphysical γ values ranging from $-75\,000 < \gamma < 240\,000\,{\rm K},$ though approximately 70% were between 0 and 1200 K. The relationship between $\Delta T_{\rm cal}$, γ , and $T_{\rm err}$ (Fig. 6) indicates that $T_{\rm err}$ is significantly reduced (darker symbols) when $\Delta T_{\rm cal} \gtrsim 1.25^{\circ}{\rm C}$ [as Eq. (5) was better constrained] with $T_{\rm err}=0.2^{\circ}\pm0.16^{\circ}{\rm C}.$ Further, high $T_{\rm err}$ is likely if $\gamma \lesssim 300\Delta$. Identifying and excluding data when γ is in a range that results in high error at a

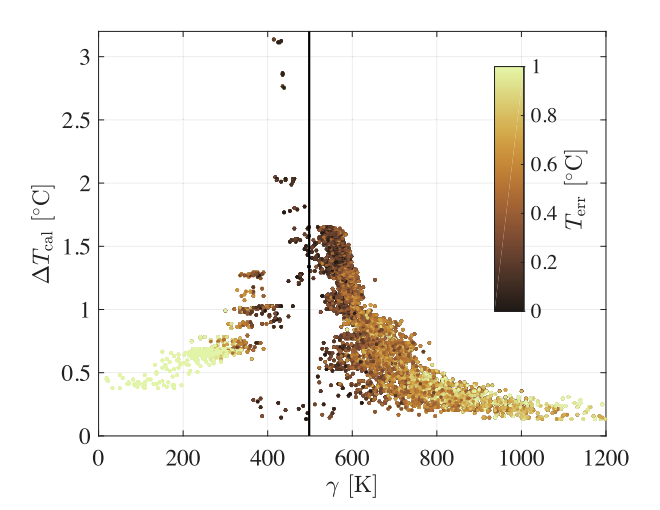


FIG. 6. Calibration section minimum temperature difference $\Delta T_{\rm cal}$ vs calibration parameter γ [from poorly constrained Eq. (5)] and temperature error $T_{\rm err}$ (color bar) at each validation point along the cable. The empirically determined constant $\gamma=498\,{\rm K}$ is highlighted (vertical line).

validation point is one proven quality control method (Connolly and Kirincich 2019). Independently estimating one of the free parameters in Eq. (5), as described below, is another option.

2) Options for Calibrating with small $\Delta T_{\rm cal}$

The differential attenuation parameter $\Delta \alpha$ can be independently estimated if temperature along a section is constant (e.g., Hausner et al. 2011; van de Giesen et al. 2012). However, long calibration lengths at a known temperature are not always available in the field, and as discussed in section 3b, coils, crimps, and other cable stresses can cause variations in $\Delta \alpha$ along the cable. The parameter C is unique to the DTS instrument and setup. So, independently estimating γ [Eq. (4)] may be a good choice when long, straight, temperature controlled calibration lengths are not available. Since ΔE is a nearly constant function of the cable material quantum states, roughly 50 meV for SiO₂ (Farahani and Gogolla 1999), γ is nearly constant as well, though small γ variations may be caused by the laser system, instrument power and temperature (van de Giesen et al. 2012). When $\gamma \approx 500 \, \text{K}$ (near the theoretical value for a SiO₂ fiber), $T_{\rm err}$ was low even when $\Delta T_{\rm cal}$ was small (Fig. 6).

If a theoretical γ value is not known, it is possible to empirically estimate γ , then recalibrate the DTS temperature using this value. Restricting observations to when $\Delta T_{\rm cal} > 1.25^{\circ}{\rm C}$, then taking a mean value weighted by $\Delta T_{\rm cal}$ gives an empirical estimate of $\gamma = 498\,{\rm K}$ (vertical line, Fig. 6), within 5% of the theoretical value. Empirically estimating γ in this way requires no extra validation points and restricts γ to physically significant values.

3) Calibration with constant γ

Applying a theoretically or empirically determined constant γ when $\Delta T_{\rm cal}$ was low and recalibrating temperature from Eq. (5) using three reference sections (now an overdetermined problem) significantly reduced DTS temperature error along the entire length of the cable from $T_{\rm err}=1.22^{\circ}\pm44.23^{\circ}{\rm C}$ to $T_{\rm err}=0.17^{\circ}\pm0.14^{\circ}{\rm C}$. Calibration using a constant γ was comparable to calibration results from a temperature controlled ice bath (triangles, Fig. 5). An additional \approx 0.1°C bias was observed near the calibration section end of the cable (decreasing down the cable length) using this method (squares, Fig. 5). However, maintaining $\Delta T_{\rm cal}>1.25^{\circ}{\rm C}$ and restricting γ to physical values [resolving the overdetermined Eq. (5)] allows DTS calibration with minimal additional error when $\Delta T_{\rm cal}$ is small.

c. Loss of the terminal calibration section

In the field, the terminal calibration section (at the end of the cable) is usually deployed from a ship in dynamic seas onto an unknown bottom condition. The cable itself is subject to damage during the deployment, and terminal calibration thermistors can become lost or damaged, complicating calibration with the standard method. In these situations, the DTS may still generate good data, but an alternative calibration is required. Frequently, validation thermistors are attached along the cable which can be substituted for a calibration section in this circumstance. In this case, calibration would be

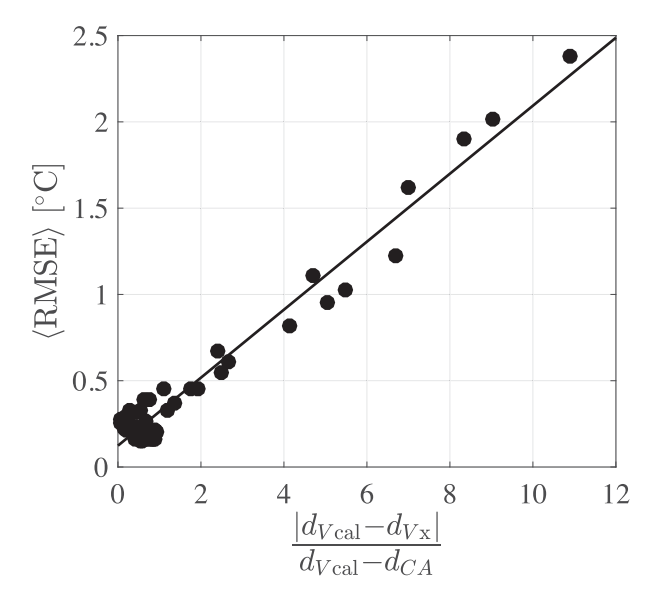


FIG. 7. Time-averaged validation point root-mean-square error $\langle RMSE \rangle$ for all possible calibration configurations (replacing CT with validation points V1 through V7) vs the ratio of distances in Eq. (7). The best fit slope is 0.20 and intercept is 0.12°C.

made using a single point (see section 5a) and at a location different from the terminal end. Here, we test this alternative calibration using the AC cable and standard ice and warm calibration sections (CI and CA), but replacing the terminal calibration point CT with validation points V1–V7 (see Fig. 2a).

The seven validation thermistors V1 to V7 placed along the AC cable, plus the terminal calibration thermistor CT provide eight locations (between d=189 and 2000 m) where the alternative terminal calibration section can be located for this test (Fig. 2a). For convenience, we term the location of the substituted validation point $d_{\rm Vcal}$. In each case, the remaining seven thermistors along the cable (at locations termed $d_{\rm Vx}$) are available to test the DTS RMSE. Thus, a ratio of two distances is defined based on the choice of alternative terminal calibration point,

$$\frac{|d_{\text{Vcal}} - d_{\text{Vx}}|}{d_{\text{Vcal}} - d_{\text{CA}}}.$$
 (7)

Here, the numerator is the positive distance between the substituted validation point d_{Vcal} (used for terminal calibration) and another validation point. The denominator is the distance between d_{Vcal} and the next nearest calibration bath, in this case CA. Thus, the ratio in Eq. (7) at a given location is small when the distance between calibration sections is large, and the cable location is near a calibration point. Calibrations were made substituting validation points V1 through V7 for CT, and the time-averaged $\langle \mathrm{RMSE} \rangle$ was found at all other validation points for each subsequent calibration.

A strong linear relationship exists ($R^2 = 0.96$) between $\langle RMSE \rangle$ and the ratio of distances in Eq. (7) (Fig. 7). Though each DTS system and cable setup is different, the 0.20°C slope provides guidance for expected DTS error along the cable if

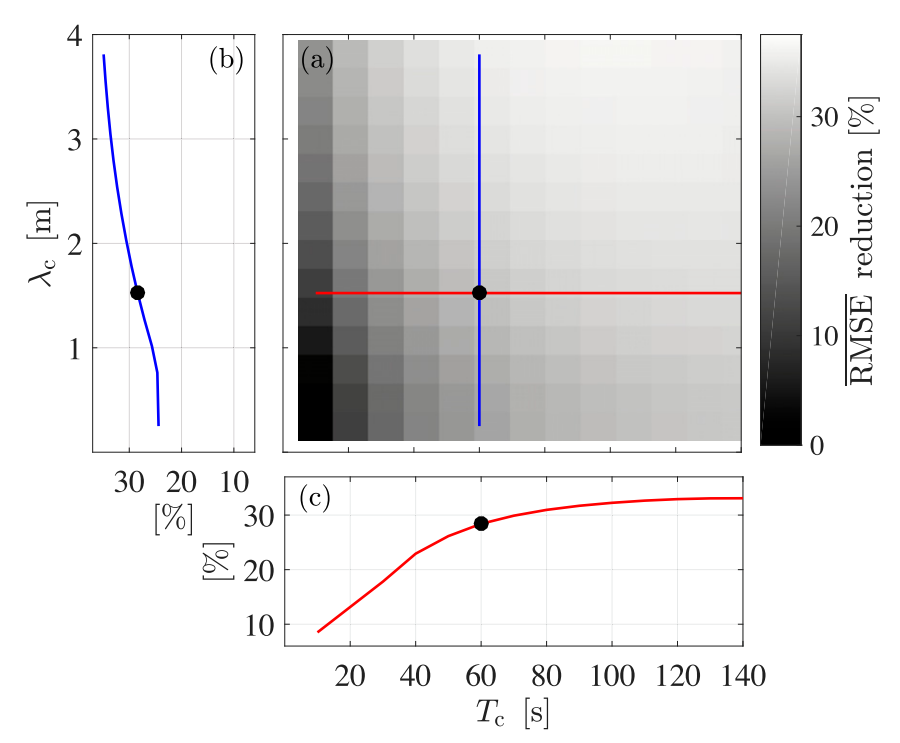


FIG. 8. (a) Reduction in DTS temperature RMSE averaged over all validation points ($\overline{\text{RMSE}}$ reduction, color bar) after low-pass filtering at various spatial (λ_c , ordinate) and temporal (T_c , abscissa) cutoff values. Cross sections through the response surface highlight (b) the generalized spatial averaging effect (blue) at constant T_c and (c) the generalized temporal averaging effect (red) at constant λ_c . The optimized filtering location (black dot) maximizes $\overline{\text{RMSE}}$ reduction while retaining the highest spatial and temporal resolutions.

calibration at large d is unavailable and alternative calibration using a validation point at some smaller d is required. The best fit intercept of 0.12°C (Fig. 7) is the expected $\langle RMSE \rangle$ under optimal calibration conditions. Reducing this error is the subject of section 6a.

6. Data processing

a. Noise reduction

Significant signal processing is internal to the Silixa DTS systems used in this experiment, and the signal quality will undoubtedly improve as technology matures. Regardless, the DTS user may ultimately wish to reduce noise by temporally and spatially averaging or filtering (e.g., Connolly and Kirincich 2019; Reid et al. 2019), while retaining as much spatial and temporal resolution as possible. Here, postprocessing techniques to reduce RMSE are quantified with respect to the loss in spatial and temporal resolution.

The Silixa XT-DTS sampled the FC cable (Fig. 2b) during the same three day period as in section 3b with 10 s acquisition time and 0.25 m spatial resolution. The DTS signal was calibrated using 10 m long ice, ambient, and terminus calibration sections (CI, CA, and CT, respectively, Fig. 2b) following section 3b. The nine validation thermistors located along the cable provided independent and highly accurate temperature measurements.

Temperature at validation sites (V1 to V9 in Fig. 2b) is compared with DTS temperature at a colocated cable section. At each location, a linear fit to the 3 days of data yield the bias, best-fit slope, and RMSE from the predicted value. DTS temperature observations were smoothed in several ways to test postprocessing noise reduction methods. First, successive observations (in time and space) were averaged and compared to filtered (low-pass sixth-order Butterworth) observations. Carefully averaging, either by selecting a longer acquisition time or in postprocessing, is typical (Selker et al. 2014), though no significant RMSE difference existed between data processed with comparably sized filter cutoff and averaging windows. Second, raw Stokes and anti-Stokes returns were filtered and used for calibration, then compared with filtered temperature data processed from unfiltered returns. Again, no significant RMSE reduction difference was observed. Filtering the raw Stokes and anti-Stokes signal before subsequent processing, as if the DTS user had selected a different acquisition time and spatial resolution a priori, is done for the remainder of this analysis.

Filter lengths from 0 to 150 s and from 0 to 4 m were applied to the DTS data and compared to the similarly filtered (in time only) validation points. This experimental design generated a response surface (e.g., Montgomery 2013) relating \overline{RMSE} reduction to filter choice (Fig. 8a). For each combination of temporal and spatial filtering, and at each validation location,

the best fit slope was within 6% of unity, indicating consistent calibration. The bias was similarly consistent and was unaffected by the filtering choice.

Filtering at high temporal and spatial cutoffs reduced the $\overline{\rm RMSE}$ as much as 35% (Fig. 8a), though the individual RMSE response related to temporally or spatially filtering were different. Temporally filtering the DTS signal significantly improved RMSE, though there was little additional RMSE improvement when $T_c > 80\,\mathrm{s}$ (Fig. 8c). Spatially filtering the DTS signal contained a similar square root functional relationship, but was generally less effective at reducing RMSE than temporally averaging (Fig. 8b). It is notable that validation points cannot be smoothed over distance, so comparison between spatially smoothed DTS data and validation points also depends on the spatial scale of inherent temperature features (here $\approx 40\,\mathrm{m}$, see section 6b).

Selecting spatial and temporal averaging or filtering scales depends on the required temperature and observational resolution of the field study. Generally, however, a DTS user would like to reduce as much error as possible while retaining the best possible temporal and spatial resolution. This optimization problem is addressed here by locating the point on the 2D response surface (color bar, Fig. 8a) with maximum Gaussian curvature (e.g., Goldman 2005). With no filter preference (e.g., the surface axes are weighted equally), the optimal filtering combination is achieved when $\lambda_c = 1.5 \, \mathrm{m}$ and $T_c = 60 \, \mathrm{s}$ (black dot, Fig. 8). Under these conditions, RMSE improved by 32.5%. The cable response time limits temporal resolution (section 4) and should be considered when choosing an averaging or acquisition time.

b. Boundary interface location

DTS deployments may often require the cable to pass through boundaries of different temperature regimes. For example, DTS deployments in tidal estuaries may be shallow enough to allow the cable to be occasionally exposed to air (Harvey 2019). Observations of snow and ice may require the cable to pass through the ice/water/land boundary at an unknown cable location (e.g., Tyler et al. 2008). Dense armored cables may become buried if deployed on loose substrates. At some point, all oceanographic DTS cables must enter the water, and this interface can have different temperature properties (Selker et al. 2006b). Determining this boundary location along the cable is sometimes possible by inspection at deployment and can be important both scientifically and for data quality control. However, difficult or changing environmental conditions may require a boundary location to be estimated from the temperature data themselves.

Temperature in regions with different thermal properties is often forced by different processes and is sensed differently by the cable (see section 4). A boundary location (for instance between ice and water) may be identifiable from thermal gradient changes (e.g., Kobs et al. 2014). When thermal gradient changes are not apparent, hypothesis testing on the temperature variance may help determine if separate DTS cable sections are sampling fluid from different regions. For a robust statistical test on the variance, test samples should have Gaussian temperature distributions. Thus, the two test samples

should be taken within the decorrelation length scale of the expected temperature variance. For example, locations at $d=300\,\mathrm{m}$ and $d=1500\,\mathrm{m}$ may both be in the water (see Fig. 1) but ocean temperature at these locations may not be correlated. Internal waves and other nearshore processes affecting this site reduce temperature correlation beyond a spatial lag of \approx 40 m (Sinnett et al. 2018). Air temperature is correlated at longer scales. Here, we select sample locations separated by 10 m, which largely have correlated temperature fluctuations and similar variance, provided both sample locations are either in water or in air. Additionally, we select a time series length that is short compared to the dominant temperature variability scale. Here, for example, dominant temperature variability is near semidiurnal frequencies (Fig. 3) so a sample length less than 1 h is selected.

To identify an interface, the temperature variance at each sample location (separated here by 10 m) is tested for statistical similarity using, for example, a χ^2 variance test or F test (e.g., Emery and Thomson 2001). If the temperature variance is statistically similar, the two sample locations are likely sampling the same material (water, for example). By then incrementally shifting the sample locations along the cable, eventually the two locations straddle an interface and the temperature variance may become statistically different (here above the 95% confidence interval). The interface location can be confirmed by continuing to sample incrementally along the cable until both locations again have statistically similar variance (both are sampling air, for example). An interface is detected when the first and last statistically significant samples occur at the sample separation distance, here 10 m. This method correctly identified both the air/sea interface and locations where the cable was significantly buried in the sand, as confirmed by dives on 26 October, 29 October, and 4 November.

7. Summary

Distributed temperature sensing (DTS) is an emerging oceanographic tool capable of observing temperature across wide spatial and temporal scales. Using this delicate instrument in remote and dynamically complex ocean settings is challenging, and achieving best practices for DTS deployment and calibration are sometimes impossible. This experiment used multiple DTS instruments and fibers (Figs. 1 and 2) configured to test several likely oceanographic complications regarding DTS deployment, calibration (sections 3b and 5) and data processing (section 6).

Coiling fiber optic cable is common for calibration, but deploying cable in dynamic oceanographic settings often adds additional strain, bends, and crimps at points along the cable, causing attenuation $\Delta\alpha$ to vary. A piecewise linear $\Delta\alpha$ correction for a single-ended cable was made using long time averages [Eq. (6)]. Sections were selected such that most of the bends, coils and stress points affecting $\Delta\alpha$ were partitioned in one section. This first-order $\Delta\alpha$ correction reduced temperature bias by nearly 0.3°C (section 3b) for a single-ended configuration.

The cable response time (section 4) and other experimental considerations factor into deployment options, DTS sampling

configuration and postprocessing optimization. Once deployed, calibration with cable sections in a known temperature bath is recommended. However, calibration using a single point is possible (see section 5a) if sections are unavailable. Single point calibration slightly increased RMSE, with the largest error in sections of the cable where P_S returns were small (i.e., generally at larger d, Fig. 4).

Optimal calibration temperatures required to constrain Eq. (3) or Eq. (5) are often provided by an ice bath and warmer bath (usually ambient). DTS temperature error can be large when calibration temperature differences $\Delta T_{\rm cal}$ are small and calibration routines are not adjusted. When $\Delta T_{\rm cal} < 1.25^{\circ}{\rm C}$, observed RMSE was at times above 30°C (section 5b). However, when $\Delta T_{\rm cal}$ is small, holding γ constant, either at a known theoretical value or a value determined from empirical estimation (as in section 5b), reduced temperature error and bias along the cable length comparable to calibration with large $\Delta T_{\rm cal}$ (Fig. 5).

Damaging the DTS cable or losing calibration instruments is possible in dynamic ocean regions or on rough bottom topography. In this case, alternative calibration using a thermistor intended for validation (rather than the terminal calibration section) is possible, potentially increasing RMSE. DTS temperature RMSE was linearly related to the distance ratio between a point on the cable and the nearest calibration section, and the largest distance between calibration sections (section 5c and Fig. 7). Error at a cable location was minimized by constraining the distance from a calibration section or increasing the distance between calibration sections.

Broad temporal and spatial temperature resolution is a primary DTS feature, though inherent noise is a challenge. Spatially or temporally averaging (or filtering) the P_S and P_{aS} signal reduced noise, but also reduced the high frequency and small spatial scale resolution. Due to inherent DTS and optical factors, choosing the longest possible sampling acquisition time and distance is the most effective noise reduction method, with precision increasing as the square root of integration interval (Selker et al. 2006b). Here, RMSE improvements from temporal and spatial filtering are benchmarked (section 6a and Fig. 8).

Detecting the air/sea boundary from DTS data is a challenge in deployments where water level changes (e.g., due to tides, waves, surge etc.) can expose the cable. A procedure to statistically test the temperature variance between two locations (section 6b) effectively identified the air–sea interface, and is applicable in other cases containing a boundary between regions of different temperature characteristics.

Acknowledgments. This publication was prepared under NSF Grant OCE-1753317. AJL and associated technical staff were supported by Office of Naval Research Grants N00014-15-1-2876 and N0014-15-1-2529. We thank Rich Walsh for logistical, diving, and small craft operational support. Sarah Merrigan, Aryan Safaie and Derek Grimes helped prepare, deploy, and recover the DTS cables. Duncan Wheeler assisted with diving surveys, and Mike Goldin and San Nguyen provided DTS instrumentation support. Falk Feddersen lent several thermistors to this project. We would also like to thank

and acknowledge John Selker, Scott Tyler, Cara Walter, Christopher Kratt, and the Center for Transformative Environmental Monitoring Programs (CTEMPS, NSF EAR Awards 1440596 and 1440506). Three anonymous reviewers contributed helpful suggestions.

Data availability statement. In accordance with AMS policy, data are available at https://sandbox.zenodo.org/record/534994. Please email gsinnett@uci.edu for further details.

REFERENCES

- Alberty, M. S., S. Billheimer, M. M. Hamann, C. Y. Ou, V. Tamsitt, A. J. Lucas, and M. H. Alford, 2017: A reflecting, steepening, and breaking internal tide in a submarine canyon. *J. Geophys. Res. Oceans*, 122, 6872–6882, https://doi.org/10.1002/2016JC012583.
- Arnon, A., J. Selker, and N. Lensky, 2014: Correcting artifacts in transition to a wound optic fiber: Example from high-resolution temperature profiling in the Dead Sea. *Water Resour. Res.*, **50**, 5329–5333, https://doi.org/10.1002/2013WR014910.
- Connolly, T. P., and A. R. Kirincich, 2019: High-resolution observations of subsurface fronts and alongshore bottom temperature variability over the inner shelf. *J. Geophys. Res. Oceans*, **124**, 593–614, https://doi.org/10.1029/2018JC014454.
- Curtis, A., and P. Kyle, 2011: Geothermal point sources identified in a fumarolic ice cave on Erebus volcano, Antarctica using fiber optic distributed temperature sensing. *Geophys. Res. Lett.*, **38**, L16802, https://doi.org/10.1029/2011GL048272.
- Davis, K. A., R. S. Arthur, E. C. Reid, J. S. Rogers, O. B. Fringer, T. M. DeCarlo, and A. L. Cohen, 2020: Fate of internal waves on a shallow shelf. *J. Geophys. Res. Oceans*, 125, e2019JC015377, https://doi.org/10.1029/2019JC015377.
- Emery, W. J., and R. E. Thomson, 2001: *Data Analysis Methods in Physical Oceanography*. Elsevier, 638 pp.
- Farahani, M., and T. Gogolla, 1999: Spontaneous Raman scattering in optical fibers with modulated probe light for distributed temperature Raman remote sensing. *J. Lightwave Technol.*, **17**, 1379–1391, https://doi.org/10.1109/50.779159.
- Goldman, R., 2005: Curvature formulas for implicit curves and surfaces. Comput. Aided Geom. Des., 22, 632–658, https:// doi.org/10.1016/j.cagd.2005.06.005.
- Harvey, M., 2019: Hydrodynamics in intermittently closed estuaries over multiple timescales and varying forcing conditions. Ph.D. thesis, University of California, San Diego, 172 pp., https://escholarship.org/uc/item/20779367.
- Hausner, M. B., and S. Kobs, 2016: Identifying and correcting step losses in single-ended fiber-optic distributed temperature sensing data. J. Sens., 2016, 7073619, https://doi.org/10.1155/ 2016/7073619.
- —, F. Suárez, K. E. Glander, N. Giesen, J. S. Selker, and S. W. Tyler, 2011: Calibrating single-ended fiber-optic Raman spectra distributed temperature sensing data. *Sensors*, 11, 10859–10879, https://doi.org/10.3390/s111110859.
- Henderson, R. D., F. D. Day-Lewis, and C. F. Harvey, 2009: Investigation of aquifer-estuary interaction using wavelet analysis of fiber-optic temperature data. *Geophys. Res. Lett.*, 36, L06403, https://doi.org/10.1029/2008GL036926.
- Kobs, S., D. M. Holland, V. Zagorodnov, A. Stern, and S. W. Tyler, 2014: Novel monitoring of Antarctic ice shelf basal melting using a fiber-optic distributed temperature sensing mooring. *Geophys. Res. Lett.*, 41, 6779–6786, https://doi.org/10.1002/2014GL061155.
- Montgomery, D. C., 2013: *Design and Analysis of Experiments*. 8th ed. John Wiley and Sons, 752 pp.

- Neilson, B. T., C. E. Hatch, H. Ban, and S. W. Tyler, 2010: Solar radiative heating of fiber-optic cables used to monitor temperatures in water. *Water Resour. Res.*, 46, W08540, https:// doi.org/10.1029/2009WR008354.
- Read, T., and Coauthors, 2013: Characterizing groundwater flow and heat transport in fractured rock using fiber-optic distributed temperature sensing. *Geophys. Res. Lett.*, 40, 2055–2059, https://doi.org/10.1002/grl.50397.
- Reid, E. C., T. M. DeCarlo, A. L. Cohen, G. T. F. Wong, S. J. Lentz, A. Safaie, A. Hall, and K. A. Davis, 2019: Internal waves influence the thermal and nutrient environment on a shallow coral reef. *Limnol. Oceanogr.*, 64, 1949–1965, https://doi.org/ 10.1002/lno.11162.
- Selker, J., N. van de Giesen, M. Westhoff, W. Luxemburg, and M. B. Parlange, 2006a: Fiber optics opens window on stream dynamics. *Geophys. Res. Lett.*, 33, L24401, https://doi.org/ 10.1029/2006GL027979.
- —, and Coauthors, 2006b: Distributed fiber-optic temperature sensing for hydrologic systems. Water Resour. Res., 42, W12202, https://doi.org/10.1029/2006WR005326.
- —, S. Tyler, and N. van de Giesen, 2014: Comment on "Capabilities and limitations of tracing spatial temperature patterns by fiber-optic distributed temperature sensing" by Liliana Rose et al. Water Resour. Res., 50, 5372–5374, https:// doi.org/10.1002/2013WR014979.
- Shanafield, M., E. W. Banks, J. W. Arkwright, and M. B. Hausner, 2018: Fiber-optic sensing for environmental applications: Where we have come from and what is possible. *Water Resour. Res.*, 54, 8552–8557, https://doi.org/10.1029/2018WR022768.

- Sinnett, G., F. Feddersen, A. J. Lucas, G. Pawlak, and E. Terrill, 2018: Observations of nonlinear internal wave run-up to the surfzone. J. Phys. Oceanogr., 48, 531–554, https://doi.org/ 10.1175/JPO-D-17-0210.1.
- Tyler, S. W., S. A. Burak, J. P. McNamara, A. Lamontagne, J. S. Selker, and J. Dozier, 2008: Spatially distributed temperatures at the base of two mountain snowpacks measured with fiber-optic sensors. J. Glaciol., 54, 673–679, https://doi.org/10.3189/002214308786570827.
- —, J. S. Selker, M. B. Hausner, C. E. Hatch, T. Torgersen, C. E. Thodal, and S. G. Schladow, 2009: Environmental temperature sensing using Raman spectra DTS fiber-optic methods. *Water Resour. Res.*, 45, W00D23, https://doi.org/10.1029/2008WR007052.
- —, D. M. Holland, V. Zagorodnov, A. A. Stern, C. Sladek, S. Kobs, and J. Bryenton, 2013: Using distributed temperature sensors to monitor an Antarctic ice shelf and sub-iceshelf cavity. *J. Glaciol.*, **59**, 583–591, https://doi.org/10.3189/ 2013JoG12J207.
- van de Giesen, N., S. C. Steele-Dunne, J. Jansen, O. Hoes, M. B. Hausner, S. Tyler, and J. Selker, 2012: Double-ended calibration of fiber-optic Raman spectra distributed temperature sensing data. *Sensors*, **12**, 5471–5485, https://doi.org/10.3390/s120505471.
- Zeeman, M. J., J. S. Selker, and C. K. Thomas, 2015: Near-surface motion in the nocturnal, stable boundary layer observed with fibre-optic distributed temperature sensing. *Bound.-Layer Meteor.*, **154**, 189–205, https://doi.org/10.1007/s10546-014-9972-9.